



ASME Accepted Manuscript Repository

Institutional Repository Cover Sheet

Ecole Polytechnique Fédérale de Lausanne, Switzerland  
Infoscience (<https://infoscience.epfl.ch/>)  
<https://infoscience.epfl.ch/record/271135?ln=en>

Patrick Hubert Wagner

Wagner

[mail@patrick-wagner.net](mailto:mail@patrick-wagner.net)

*First*

*Last*

*E-mail*

**ASME Paper Title:** Theoretical and Experimental Investigation of a Small-Scale, High-Speed, and Oil-Free Radial

Anode Off-Gas Recirculation Fan for Solid Oxide Fuel Cell Systems

**Authors:** Patrick Hubert Wagner, Jan Van herle, Jürg Schiffmann

**ASME Journal Title:** Journal of Engineering for Gas Turbines Power

**Volume/Issue:** 142/4

**Date of Publication (VOR\* Online):** February 14, 2020

**ASME Digital Collection URL:**

<https://asmedigitalcollection.asme.org/gasturbinespower/article/doi/10.1115/1.4045104/1065414/Theoretical-and-Experimental-Investigation-of-a>

**DOI:** <https://doi.org/10.1115/1.4045104>

\*VOR (version of record)

**POST-PRINT: THEORETICAL AND EXPERIMENTAL INVESTIGATION OF A  
SMALL-SCALE, HIGH-SPEED, AND OIL-FREE RADIAL ANODE OFF-GAS  
RECIRCULATION FAN FOR SOLID OXIDE FUEL CELL SYSTEMS**

**Patrick H. Wagner\***

Laboratory for Applied Mechanical Design  
Institute of Mechanical Engineering  
École Polytechnique Fédérale de Lausanne  
Neuchâtel, Neuchâtel, 2000  
Switzerland  
Email: patrick.wagner@epfl.ch

**Jan Van herle**

Group of Energy Materials<sup>†</sup>  
IGM  
EPFL  
Sion, Valais, 1951  
Switzerland  
Email: jan.vanherle@epfl.ch

**Jürg Schiffmann**

LAMD  
IGM  
EPFL  
Neuchâtel, Neuchâtel, 2000  
Switzerland  
Email: jurg.schiffmann@epfl.ch

**ABSTRACT**

*The Laboratory for Applied Mechanical Design (LAMD) designed, manufactured, and experimentally tested a novel recirculation fan for a 10 kW<sub>e</sub> solid oxide fuel cell (SOFC). The fan uses oil-free bearings, more specifically herringbone-grooved journal and spiral-grooved thrust gas bearings. The radial inducer-less fan with a tip diameter of 19.2 mm features backward-curved prismatic blades with constant height. Prior to coupling the recirculation fan with the SOFC, the fan was experimentally characterized with air at 200 °C. At the nominal point of 168 krpm, the measured inlet mass flow rate is 4.9 kg h<sup>-1</sup>, the total-to-total pressure rise 55 mbar, the isentropic total-to-total efficiency 55 %, and the power 18.3 W. This paper compares the experimental data towards a computational fluid dynamic simulation of the full fan impeller and volute suggesting an excellent correlation at the nominal point what validates the numerical approach. However, the heat flows crossing the fan fluid domain, have an increased effect at off-design conditions, thus the experimental results need careful consideration. The fan backface leakage has negligible impact on the measurements.*

**NOMENCLATURE**

*b* (Channel) width m  
*c* Clearance in m  
*d, D* Diameter in m  
*h* Specific enthalpy in J kg<sup>-1</sup> K<sup>-1</sup>  
*g* Gravitational acceleration m s<sup>-2</sup>  
*l* Length in m  
*M* Torque in Nm  
*m* Mass flow rate in kg s<sup>-1</sup>  
*P* Power in W

\*Address all correspondence to this author.

<sup>†</sup>Since September 26, 2016; formerly JVH Fuelmat Group

$p$  Pressure in Pa  
 $\dot{Q}$  Heat rate in W  
 $T$  Temperature in K  
 $t$  (Blade) thickness in m  
 $\beta$  Blade angle based on the circumference in  $^\circ$   
 $\gamma$  Molar fraction  
 $\eta$  Efficiency  
 $\omega$  Angular speed in  $\text{rad s}^{-1}$

#### Subscript

1 machine inlet / inlet side test section  
2 inducer inlet  
3 fan blade leading edge  
4 fan blade trailing edge  
8 machine outlet / outlet side test section  
a axial  
amb ambient  
cond conduction  
e electrical  
h housing  
is isentropic  
l leakage  
n nominal  
s shroud  
st static  
t total

#### Abbreviation

AOR anode off-gas recirculation  
CFD computational fluid dynamics  
DLC diamond-like carbon  
HGJB herringbone-grooved journal bearing  
LE leading edge  
TE trailing edge  
SOFC solid oxide fuel cell  
SGTB spiral-grooved thrust bearing

## INTRODUCTION

Intermediate-temperature solid oxide fuel cells (SOFCs) have proven to be efficient and reliable: The commercial product BlueGEN with a net output power of  $1.5 \text{ kW}_e$  reaches net efficiencies based on the lower heating value of methane of 60 % and utilization ratios that take into account the cogeneration of electricity and low-temperature heat of 85 % [1]. An SOFC prototype equipped with a similar technology as used by the BlueGEN has achieved recently more than 90000 h of continuous operation at the German research center “Forschungszentrum Jülich” [2].

Wagner et al. [3] simulated and optimized a  $10 \text{ kW}_e$  SOFC system with anode off-gas recirculation (AOR). Their conclusion is that an electrical net efficiency of up to 64.9 % and a utilization ratio of up to 97.2 % are theoretically possible. Peters et al. [4] experimentally demonstrated the technical feasibility of a  $2.5 \text{ kW}_e$  SOFC stack with AOR reaching an electrical net efficiency of 58.5 %. They claim that if a new stack had been used instead of an aged one the efficiency would have been at least five percentage points higher. The results therefore suggest that net efficiencies on the order of 65 % are within reach for SOFC systems coupled with AOR devices. Although the mentioned SOFC systems are at domestic scale with a power output of a few  $\text{kW}_e$ , their efficiencies are comparable with state-of-the-art combined-cycle power plants, which deliver electrical power on the order of several hundreds of  $\text{MW}_e$ . As of September 2018, the world record gross efficiency for combined-cycle power plants is 63.1 % [5].

An additional advantage of the SOFC is the locally cogenerated heat, which domestic heating or cooling can use; hence, increasing the

system utilization ratio. Cogeneration of electricity and heat is very promising for decentralized energy integration in residential and commercial markets.

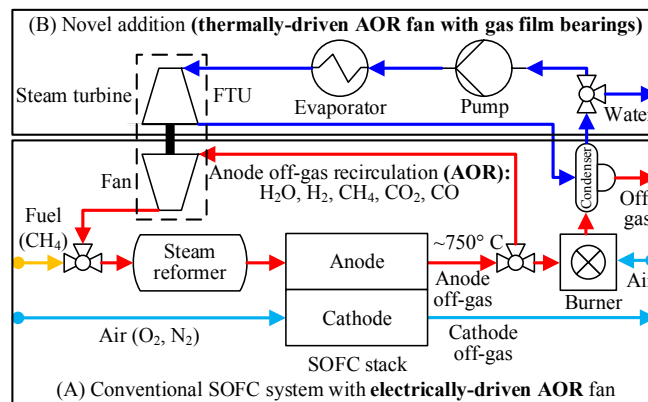
### SOFC SYSTEM WITH ANODE-OFF GAS RECIRCULATION

Figure 1 at the bottom (A) shows a conventional SOFC system with an electrically-driven AOR fan, as demonstrated by Powell et al. [6]. The incoming fuel is natural gas, which consists overall of methane ( $\text{CH}_4$ ). It is mixed with the AOR, which contains among other gases water vapor ( $\text{H}_2\text{O}$ ). This water vapor reacts with methane to hydrogen via the steam reforming and water-gas shift reaction. The products of the steam reformer are carbon monoxide ( $\text{CO}$ ), carbon dioxide ( $\text{CO}_2$ ), unreformed methane (typically part of the methane is reformed in the SOFC stack), and hydrogen. These gases are heated and enter the SOFC anode. Due to lifetime considerations, the local fuel utilization of the SOFC anode is limited. The anode off-gas therefore consists of non-reacted hydrogen ( $\text{H}_2$ ) and water vapor, which is pH-neutral and deionized. Thus, this water vapor can be used for the steam reforming process at the anode inlet. The non-reacted hydrogen in the anode off-gas is burned with fresh air and then condensed. The burner off-gas and the water exit the system in the chimney and the drain, respectively. AOR has therefore three major benefits: (1) It enables a water-neutral operation of the SOFC system, without a water treatment system for the external water supply. (2) The global fuel utilization of the SOFC system is increased due to the recirculation of non-reacted hydrogen, what increases the system efficiency. (3) The local fuel utilization of the stack is reduced, what increases the stack lifetime [3].

This paper proposes a thermally-driven AOR fan, the fan-turbine unit (FTU). Figure 1 shows this novel concept at the top (B) as an addition to the conventional SOFC system at the bottom (A). Part of the condensed water is pumped, evaporated, and expanded in a micro steam turbine. The heat from the burner off-gas is recuperated and used to evaporate the water (heat exchangers not shown in Figure 1). The steam turbine is connected by a shaft lubricated on gas film bearings with the fan. Thus, the fan is steam-driven. Since heat is recuperated to generate this steam, the fan is also thermally-driven. The turbine exhaust is fed back to the condenser.

### ANODE OFF-GAS RECIRCULATION FAN

AOR fans have special requirements due to their working environment. (1) Oil and grease-free: A pollution with oil and grease has to be avoided since it can block channels and the catalyst in the reformer and the anode, and therefore damage these components. (2) Temperature resistant: The fan has to withstand high temperatures ( $\sim 750^\circ\text{C}$ ), which corresponds to the anode off-gas temperature of an intermediate-temperature SOFC. With an additional heat exchanger (not shown in Figure 1), the anode off-gas can be cooled to simplify the fan design. The lowest AOR temperature should be above the dew point temperature of the water vapor in the anode off-gas, since condensation leads to the formation of acids. (3) Long lifetime: a typical SOFC stack is designed for an operation of five to 10 years, whereas an SOFC system can operate between 20 to 30 years. (4) No leakage to the environment, (5) explosion-proof operation, and (6) air-tightness: The anode off-gas is toxic ( $\text{CO}$ ) and explosive ( $\text{H}_2$ ). (7) Low manufacturing cost and (8) high efficiency: Reducing costs and increasing efficiency is essential for the competitiveness of the SOFC technology.



**GTP-19-1480-FIGURE 1.** FLOW SHEET OF (A) A CONVENTIONAL SOFC SYSTEM WITH AN ELECTRICALLY-DRIVEN AOR FAN AND (B) WITH A THERMALLY-DRIVEN AOR FAN, THE FAN-TURBINE UNIT (FTU).

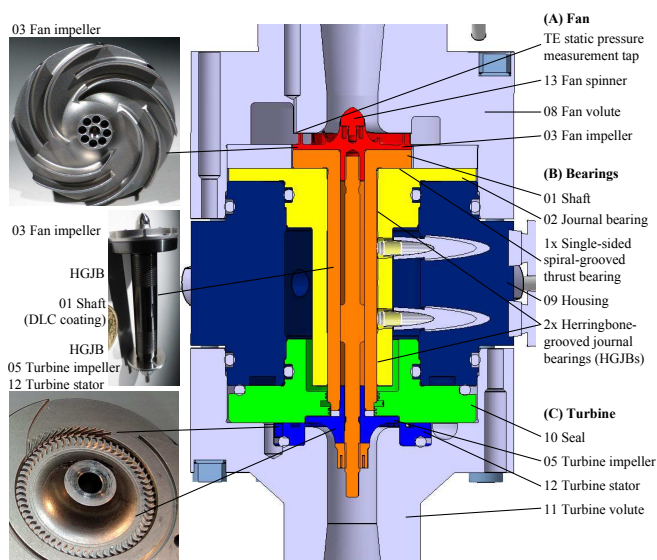
Considering electrically-driven AOR fans, the literature provides four different devices, which can be categorized in low-speed machines (1-2) and high-speed machines (3-4):

- (1) AOR fan with ball bearings that are coupled to an electric motor with a magnetic coupling: Both Powell et al. [6] and Peters et al [4] used a side channel blower with magnetic drive from Airtech West and Vacuvane, respectively. Due to the magnetic coupling, the blower is explosion-proof, but both the operation temperature (145 °C and 160 °C, respectively), as well as the maximum rotational speed are limited.
- (2) Directly coupled AOR fan with ball bearings: Tanaka et al. [7] ensure the explosion-proof operation with pressurized dry purge gas, e.g., nitrogen, that is added into the blower housing. However, such a gas is mostly not readily available for domestic SOFC installations. Due to the ball bearings limited lifetime at high speeds and high temperatures, the fan is limited in the achievable rotational speed. The specific speed according to Balje [8] is 0.3, whereas the optimal value is between 0.8 to 1.0 [3].
- (3) AOR fan lubricated on dynamic oil film bearings: Rechberger et al. [9] presented a fan for temperatures up to 600 °C and rotational speeds up to 120 krpm. Due to the oil film bearings, a high lifetime is expected, even at high temperatures and rotational speeds. However, the oil can damage the SOFC stack and the steam reformer.
- (4) AOR fan lubricated on dynamic gas film bearings: Both Agrawal et al. [10] and Heshmat et al. [11] lubricate the shaft on foil journal and thrust bearings as dynamic gas film bearings. Agrawal et al. [10] operated the AOR fan with air up to 850 °C and up to 99 krpm. The specific speed according to Balje [8] is in the optimal range (0.9).

## FAN-TURBINE UNIT

Figure 2 shows the novel steam-driven AOR fan, the fan-turbine unit, which complies with all requirements (1-8), mentioned in the previous section. It is divided into three main parts: (A) the radial 19.2 mm fan at the top (red), (B) the gas film bearings in the middle (orange and yellow), and (C) the partial admission (21 %), low-reaction (15 %), radial-inflow, 15 mm steam turbine at the bottom (light blue). The specifications and design was carried out for a 10 kW<sub>e</sub> SOFC system in close collaboration with the industrial partner SOLIDpower. The feasibility of this steam-driven AOR fan on dynamic steam-lubricated bearings was demonstrated by coupling it to a 6 kW<sub>e</sub> SOFC at the facilities of SOLIDpower in Yverdon-les-Bains, Switzerland.

During the operation with the SOFC system, neither leakage of the anode off-gas to the environment (requirement 4), nor penetration of air in the unit (requirement 6) was recorded. Due to the gas film bearings, the unit operates grease and oil-free, has a long life time, and is resistant to high temperatures (requirements 1-3). The fan inlet temperature of 200 °C at the design point is a trade-off between the maximum temperatures for the diamond-like carbon (DLC) coating of the shaft (~250 °C), the maximum temperature of



**GTP-19-1480-FIGURE 2.** THE CONCEPT OF THE FAN-TURBINE UNIT, A STEAM-DRIVEN ANODE OFF-GAS RECIRCULATION FAN WITH GAS FILM BEARINGS.

high-temperature plastics ( $\sim 260^\circ\text{C}$ ) such as PTFE, as well as the entire SOFC system design. Results by Wagner et al. [3] suggest that a low-temperature AOR at  $200^\circ\text{C}$  leads to a higher SOFC electrical net efficiency compared to a hot recirculator operating at  $\sim 750^\circ\text{C}$ . But the AOR at  $200^\circ\text{C}$  complicates the SOFC system by adding an additional heat exchanger, which cools the anode off-gas from its exhaust temperature to the AOR fan inlet temperature.

Due to the absence of any electronic components, the unit is per se explosion-proof (requirement 5). The unit consists of 14 stainless steel pieces that are manufactured with turning, milling, and surface finishing operations, i.e., grinding and honing. Since the number of components, and thus the complexity of the unit is low, the manufacturing costs are low (requirement 7). A DLC coating protects the 8 mm shaft to reduce the friction and wear during the fan startup and shutdown. The rotor features two herringbone-grooved journal bearings (HGJB) and one single-sided spiral groove thrust bearing (SGTB), which are both manufactured with laser. The SGTB is located on the fan backside (not visible in Figure 2). The thrust bearing operates in the pump-in mode, i.e., it draws the gaseous lubricant from the blade TE into the fan housing. The thrust bearing clearance ( $c_a$ ) depends on the fluid, the axial load, and the thrust bearing geometry. This clearance has a measured value between 0 (before the thrust bearing lift-off) and up to  $11\ \mu\text{m}$  (measured with ambient air as lubricant). The journal bearing clearance (on the diameter) is on the order of  $10\ \mu\text{m}$  and the measured orbits are up to  $2\ \mu\text{m}$  (measured with ambient air as lubricant). Due to the small bearing clearances, the blade tip clearance of both fan and turbine can be low (design fan blade tip clearance is  $50\ \mu\text{m}$ ), what leads to improved turbomachinery efficiency, especially at small-scale (requirement 8).

## ANODE OFF-GAS RECIRCULATION FAN DESIGN

A similar methodology as presented by Wagner et al. [3, 12] is used to define the AOR radial fan design. A multi-objective optimization of an entire  $10\ \text{kW}_e$  SOFC system with respect to electrical net efficiency and utilization ratio finds the fan trailing edge (TE) diameter ( $d_4 = 19.2\ \text{mm}$ ) and the design rotational speed of 175 krpm. This corresponds to a specific speed of 0.8, as defined by Balje [8]. The integrated approach also allows to identify the fan inlet parameters: a total pressure (1.05 bar), a total temperature ( $200^\circ\text{C}$ ), a mass flow rate ( $\dot{m}_1 = 4.78\ \text{kg h}^{-1}$ ), and molar ratios of  $\text{H}_2\text{O}$ ,  $\text{H}_2$ ,  $\text{CO}$ , and  $\text{CO}_2$  (61.4 %, 7.4 %, 2.6 %, and 28.6 %, respectively). The pressure drop in the SOFC stack and in the reformer is determined based on experience, to be 30 mbar and 20 mbar, respectively. The authors estimate the overall pressure drop in the heat exchangers upstream and downstream of the reformer and within the anode loop to be 10 mbar. In total, the AOR fan compensates for 70 mbar at the design point, thus accounting for a safety margin of an additional 10 mbar of pressure drop in the valves, bends, and piping.

The fan design is based on a trade-off between efficiency and low manufacturing cost. Table 1 list the main geometrical fan parameters, such as diameters ( $d$ ), blade angles ( $\beta$ ) based on the circumferential component, the channel width ( $b$ ), the blade thickness ( $t$ ), and clearances ( $c$ ). Figure 2 at the top left shows the manufactured and tested fan.

**Fan inlet:** At the machine inlet, the flow is accelerated within the inlet nozzle to the fan inducer. The fan spinner is designed as a tangent

**TABLE 1.** GEOMETRICAL PARAMETERS OF THE RADIAL ANODE OFF-GAS RECIRCULATION FAN.

<b>Impeller (4+4 prismatic blades)</b>			
Inducer inlet (2) at hub and shroud (s)			
$d_{2hub}$	4.08 mm	$d_{2s}$	8.22 mm
Main blade leading edge (3) at hub and shroud			
$d_{3hub}$	7.32 mm	$d_{3s}$	10.02 mm
$\beta_{3,blade}$	36° (hub) to 30° (shroud)		(blunt leading edge)
Splitter blade leading edge			
$d_{splitter}$	12.70 mm		
Main and splitter blade trailing edge (4)			
$d_4$	19.20 mm	$t_{blade}$	0.25 mm
$b_4$	1.82 mm+0.15 mm	(shimmed)	
$\beta_{4,blade}$	17°	(cut-off trailing edge)	
<b>Blade tip clearance (<math>c</math>)</b>			
$c_{design}$	0.05 mm	(design)	
$c_{shim}$	0.05 mm+0.1 mm	(shimmed)	
<b>Thrust bearing clearance</b>			
$c_a$	0-0.011 mm		(measured)

Haack profile, as shown in Figure 2 at the top (part 13). The fan flow coefficient based on the total machine inlet conditions at the design point is very low (0.033). A low-flow-coefficient fan is advantageous for an inducer-less design, as the end wall frictional losses within the blade channels are increased due to a decreased hydraulic diameter. Therefore, the fan leading edge (LE) is shifted from the inducer inlet towards the radial impeller section. This also allows for a two-dimensional prismatic blade design, which is easier to manufacture. The fan shroud changes the direction from axial to radial with a radius of 2.04 mm. At the shroud the flow accelerates, whereas the fluid decelerates at the fan hub. This velocity gradient between hub and shroud leads to large incidence angles at the blade LE, even if designed at a constant radius, and thus at a constant angular velocity. This flow phenomena is addressed by decreasing the blade LE radius at the hub, which results in lower circumferential velocities, and vice versa for the shroud. The blade LE relative angle at the hub ( $36^\circ$ ) and at the shroud ( $30^\circ$ ), as well as diameters ( $d_{3hub}$  and  $d_{3s}$ ) are designed to minimize the relative velocity, and thus the losses, as suggested by Eck [13].

**Fan impeller:** The fan features four main blades and four splitter blades. The splitter blades are placed towards the radial impeller section at a diameter of 12.70 mm. The first 22 % of the main blades with respect to the meridional coordinate are fully unloaded. Thus, the Euler work in that region is zero. The pressure therefore does not increase and the pressure difference between the blade suction and pressure sides is kept within a few millibar. This low pressure difference reduces the formation of the tip leakage vortex. Since the design relative blade tip clearance ( $c_{design}/b_4 = \frac{0.05}{1.82+0.05} = 0.0267$ ) is high, this leakage flow is dominant within the impeller. The minimum feasible blade tip clearance ( $c_{design}$ ) is limited due to manufacturing and assembly tolerances, as well as the clearance within the dynamic gas film bearings. This paper presents the results for the shimmed version with a 0.15 mm blade tip clearance ( $c_{shim}$ ), which corresponds to a safety margin of 0.1 mm with respect to the design value. The blades are non-tapered and have a thickness of 0.25 mm, limited by mechanical stress induced during the milling process. The manufacturing tool limits the radius between the blade and fan hub to 0.2 mm. The manufacturing process of the fan, volute, and impeller is simplified by keeping the blade height at a constant value of 1.82 mm.

**Fan outlet:** Since a constant channel width may cause excessive diffusion within the impeller, highly backward-curved blades limit the diffusion. The blade angle at the TE with respect to the circumference is  $17^\circ$ , and thus very low. The flow therefore exits the impeller with a high circumferential velocity component, which calls for a pinched diffuser design. A diffuser in general, but especially a pinched design complicates the fan. In addition, the Laval number with respect to the design total inlet conditions and the angular velocity at the blade TE is 0.4; hence, a diffuser-less design is viable at a cost, however, of elevated losses. As a consequence, it was decided to eliminate the diffuser.

**Fan volute:** A volute right after the fan blade TE collects the fluid. At the design point, the fluid is neither accelerated, nor decelerated and its angular momentum is constant. The volute has an easy-to-manufacture rectangular shape. At the end of the logarithmic spiral, the volute features a quadratic surface ( $6.77 \text{ mm} \times 6.77 \text{ mm}$ ), which increases towards a rectangular surface at the volute outlet ( $9.93 \text{ mm} \times 6.77 \text{ mm}$ ). According to Leidel [14], the placement of the volute tongue is a trade-off between the sound level and aerodynamic efficiency. The tongue radius ( $\phi_{tongue}$ ), defined as the angle between the end and the start of the logarithmic spiral, is  $59^\circ$ , leading to a distance between the fan TE and the tongue of 2.5 mm. After the volute, a rectangular-to-circular diffuser recovers pressure.

## MEASUREMENT SETUP

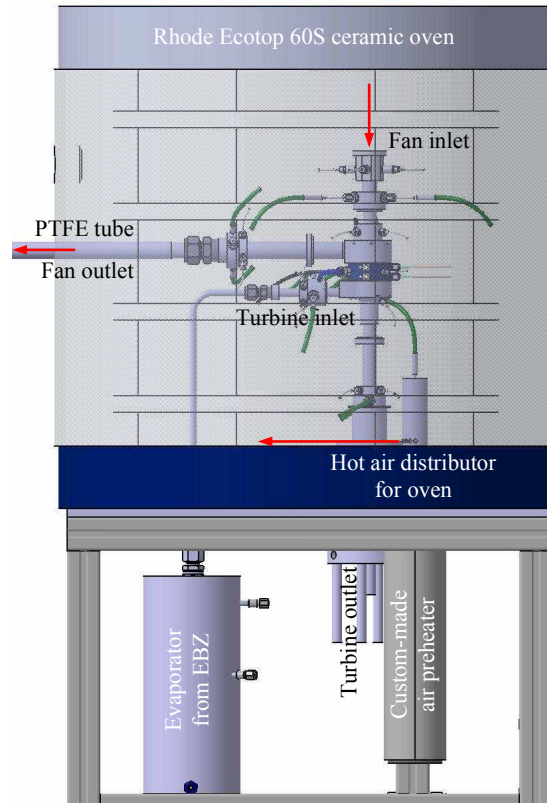
Prior to the actual coupling with the SOFC, the authors performed several experiments at their facilities: balancing of the machine up to design speed (175 krpm), measurement of thrust bearing clearance (without fan volute), fan operation with air at ambient temperature, and finally with hot air at  $200^\circ\text{C}$ . It should be noted, that the turbine is operated with hot air at  $220^\circ\text{C}$  (and thus not with steam).

Figure 3 shows the setup of the test rig using hot air at  $200^\circ\text{C}$ . The prototype with all measurement sensors is inside a ceramic oven (volume of 60 l) that maintained a constant temperature of  $200^\circ\text{C}$ , simulating the actual environment of the AOR fan in the SOFC hot box. Since the volume of the oven was small and the fan ingested hot air directly from the oven volume, an air preheating system supplied the oven with excess hot air at  $200^\circ\text{C}$ . The hot air distributor injected the preheated air into the oven parallel to the oven bottom (lowest red arrow in Figure 3) to lower the vertical temperature gradient within the oven.

The fan test setup inside the oven used the “standard test methods with outlet side test ducts - category B test installation with inlet duct (category D)” in the ISO 5801 [15]. With respect to this norm, the test rig in Figure 3 and Figure 4 featured several differences:

- Fan inlet volume flow rate measurement with a bellmouth
- Fan inlet temperature measurement (3x)
- Fan outlet temperature measurement (2x)
- No shaft torque measurement

The shaft torque measurement of such a small-device is complicated due to various reasons: (1) the shaft diameter is very small at 8 mm,



**GTP-19-1480-FIGURE 3.** OVERVIEW OF THE FAN TEST RIG FOR HOT AIR AT 200 °C (WITHOUT GLASS FIBER INSULATION).

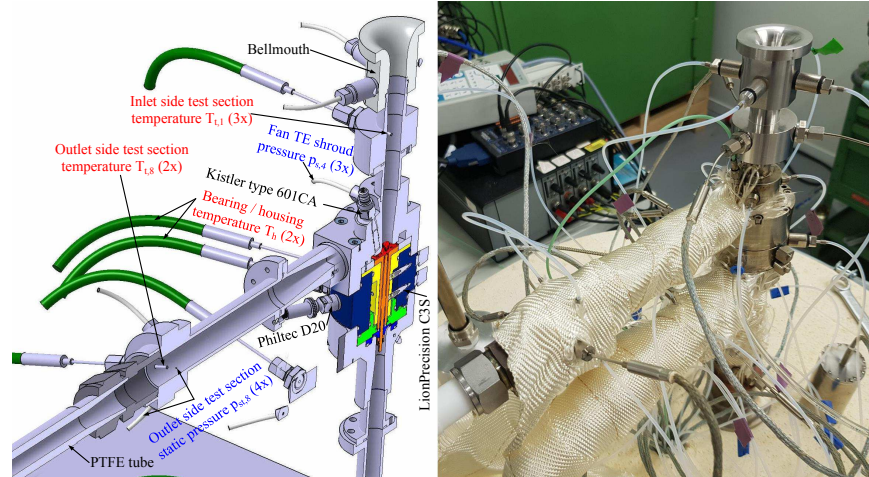
(2) the dynamic gas film bearings with a radial clearance on the order of several  $\mu\text{m}$  have a low load capacity and a low tolerance to displacement or misalignment, (3) the torque is between 0 to 0.001 N m and therefore very low, (4) the temperatures are elevated, up to 200 °C, and (5) the available area for a measurement device is restricted to a few millimeters. To the best of the authors' knowledge, no torque measurement device that complies with the above is available so far. Thus, the fan power was measured thermodynamically with the fan inlet and outlet temperatures and pressures, as well with the measured inlet mass flow rate. However, this thermodynamic measurement approach is challenging, overall for small-scale turbomachines due to: (1) high area-to-volume ratio, and thus increased heat fluxes to the environment, (2) low power (18.3 W for the investigated fan), and (3) low mechanical efficiency, and thus high heat dissipation.

Class 1 k-type thermocouples featuring 1.5 mm diameters measure the temperatures. Three evenly-distributed thermocouples are placed at  $3d_1$  ( $d_1 = 12$  mm) upstream of the fan inlet nozzle and measure the average fan inlet temperature. Two thermocouples are placed at the fan outlet after the static pressure measurement for obtaining the average fan outlet temperature (Figure 4). In order to limit the heat conduction effects between the oven environment and the thermocouples, the latter are immersed five-times their diameter into the exhaust flow. The heat conduction of the metallic outlet side test section itself to the environment is limited by decoupling it with a PTFE tube (Figures 3 and 4).

Since thermodynamic measurements determine the fan power, an adiabatic system is essential. Thus, high-temperature glass fiber insulation wrapped around the fan body and pipes inside and outside the oven limit the heat loss. Figure 4 shows these glass fiber tapes for the outlet side test section.

The test rig features four additional thermocouples: one at the top of the oven, one inside the volume flow rate measurement device in the outlet side test section (fluid outlet density calculation), and two inside the fan housing close to the journal bearings (Figure 4).

An MKS 226A (0.133 bar) differential capacitance manometer measures the differential pressure between the fan outlet (four pneumatically-averaged static pressure measurements) and the oven. A Scanivalve DSA 3218 (17.24 bar) measures the gauge pressures inside the oven, before the volume flow rate measurement device at the outlet (fluid outlet density calculation), inside the fan housing, and at the fan TE



**GTP-19-1480-FIGURE 4.** CAD OF THE FAN TEST RIG WITH MEASUREMENT POSITIONS (LEFT) AND REAL IMPLEMENTATION (RIGHT), PARTLY COVERED WITH GLASS FIBER INSULATION.

(3x). The fan volute features three evenly-distributed static pressure measurements with a diameter of 0.4 mm located at a diameter of 18.55 mm (the fan TE is 19.2 mm). The first is located at  $0^\circ$  coinciding with the end of the volute logarithmic spiral, and thus the volute outlet section (Figure 2 at the top and Figure 11). A *Lufft* Opus 20 room climate tracker measures the ambient pressure.

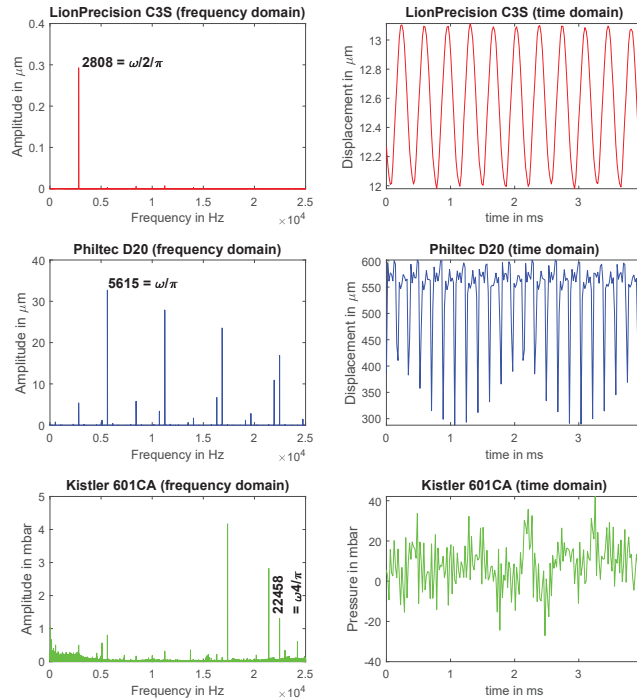
A low-ratio long radius bellmouth according to ISO 5167-3 [16] limits the pressure loss at the fan inlet. An *MKS* 223B (0.01 bar) measures the differential pressure between the bellmouth (four pneumatically-averaged static pressure measurements) and the oven environment, thus allowing to calculate the fan inlet volume flow rate ( $\dot{V}_1$ ). Since the inlet Reynolds number based on the outer bellmouth diameter ( $Re_D$ ) is smaller than the limit value in the ISO 5167 norm, the implemented bellmouth has been calibrated with the volume flow rate measurement device at the fan outlet.

An orifice plate with wall taps in accordance to ISO 5167-2 [16] measures the fan outlet volume flow rate. For low Reynolds applications, quarter circle nozzles are preferred to orifices with sharp edges such as stated within ISO 5167-2. The discharge coefficient of quarter circle nozzles is nearly constant down to Reynolds numbers based on the outer diameter ( $Re_D$ ) of 500. The VDI/VDE 2041 [17] is an addition to the ISO 5167 and states norms for such quarter circle nozzles. Like for the bellmouth at the fan inlet, the quarter circle nozzle at the fan outlet with an outer diameter ( $D_8$ ) of 12 mm is well below the minimum value in VDI/VDE 2041 (50 mm). Hence, the supplier *Tetratec* calibrated it. An *MKS* 226A (0.133 bar) measures the quarter circle nozzle differential pressure.

In order to deswirl the fan exhaust flow a cross-shaped flow straightener with a length to diameter ratio ( $l/D_8 = 24/12$ ) of 2 is placed at  $45D_8$  after the fan volute outlet diffuser, a Zanker flow conditioner plate at  $63D_8$ , and the quarter circle nozzle at  $93D_8$  (devices not

**TABLE 2.** MEASUREMENT UNCERTAINTIES.

<b>Temperature</b>		
Thermocouple	$\pm 0.5^\circ\text{C}$ , calibration (Cal.)	
<b>Pressure</b>		
<i>Scanivalve</i>	$\pm 0.018\%$ of the full scale (FS)	
<i>MKS</i>	$\pm 0.3\%$ on the read (OR)	
Ambient	$\pm 0.5$ mbar	
<b>Volume flow rate</b>		
Bellmouth	$\pm 0.96\%$ OR / $\pm 0.3\%$ OR	Cal. / <i>MKS</i>
Quarter circle nozzle	$\pm 0.91\%$ OR / $\pm 0.3\%$ OR	Cal. / <i>MKS</i>
<b>Rotational speed</b>		
<i>Philtec</i> D20	$\pm 0.5$ krpm (@ 50 kHz sampling)	
<b>Displacement</b> (max. temperature $50^\circ\text{C}$ )		
<i>LionPrecision</i> C3S	$\pm 0.25\%$ FS	



**GTP-19-1480-FIGURE 5.** ANGULAR SPEED ( $\omega$ ) AT  $17638 \text{ rad s}^{-1}$  ( $168.5 \text{ krpm}$ ) MEASURED WITH THE LIONPRECISION C3S PROBE (RED), THE PHILTEC D20 PROBE (BLUE), AND THE KISTLER 601CA (GREEN) IN THE FREQUENCY DOMAIN (LEFT) AND TIME DOMAIN (RIGHT).

visible in Figure 3).

Figure 4 shows the three measurement devices for the shaft rotational speed:

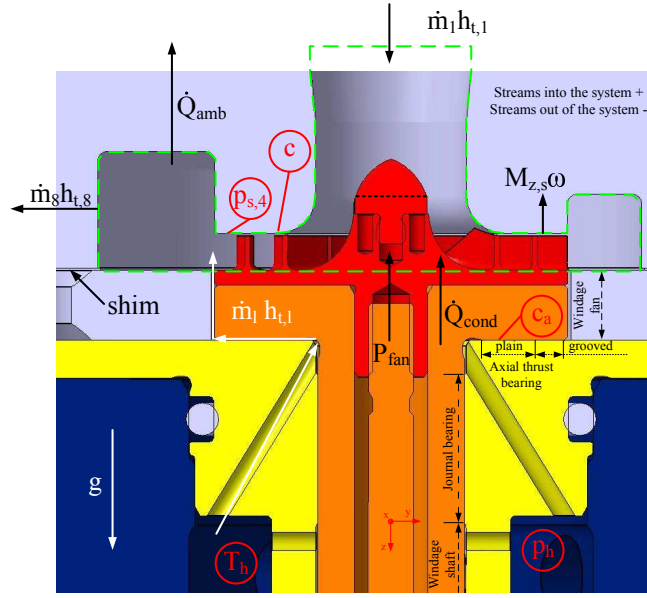
1. *LionPrecision* C3S capacitive probe (not usable at  $200^\circ\text{C}$ )
2. A high-temperature *Philtec* D20 optical probe
3. A high-temperature *Kistler* Type 601CA piezoelectric pressure sensor measuring the blade passing frequency at the blade TE (diameter of  $18.55 \text{ mm}$ )

Options 1 to 3 show coherent measurements at ambient temperatures. Figure 5 shows an example: The C3S measures the rotor orbit in one direction ( $2808 \cdot 0.06 = 168.48 \text{ krpm}$ ), the *Philtec* D20 two grooves on the shaft ( $\frac{5615}{2} \cdot 0.06 = 168.45 \text{ krpm}$ ), and the pressure sensor the blade passing frequency of the eight blades ( $\frac{22458}{8} \cdot 0.06 = 168.435 \text{ krpm}$ ). The option 2 and 3 are implemented for the measurement at high temperatures of  $200^\circ\text{C}$ .

Table 2 shows the measurement uncertainties of the temperature, pressure, volume flow rate, rotational speed, and displacement measurements. It should be noted that the measurement uncertainty of the *Scanivalve* is relatively high ( $\pm 3.1 \text{ mbar}$ ). However, both the *Scanivalve* and the *MKS* measure the fan pressure rise and both show coherent output within  $\pm 0.8 \text{ mbar}$ . The authors assume therefore the *Scanivalve* measurement accuracy as sufficient.

## FAN EFFICIENCY AND POWER MEASUREMENTS

As pointed out in the previous section, a shaft torque measurement is not possible due to several restrictions. Thus, the fan power and efficiencies are evaluated thermodynamically via the fan inlet and outlet temperatures and pressures, as well as the inlet mass flow rate. Figure 6 shows the fan impeller domain with its boundaries marked with a green-dashed line. Several enthalpy, power, and heat fluxes cross the control volume boundaries. At the fan inlet (1) and outlet (8) the measurement of mass flow rate, temperature, and pressure allow for the determination of the enthalpy.



**GTP-19-1480-FIGURE 6.** OVERVIEW OF ENTHALPY, POWER, AND HEAT INPUT / OUTPUT TO THE FAN MEASUREMENT SYSTEM.

When considering all energy fluxes shown in Figure 6, the stationary energy balance is given as follows.

$$P_{fan} + \dot{m}_1 h_{t,1} - \dot{m}_8 h_{t,8} + \dot{m}_1 h_{t,1} + \dot{Q}_{cond} - \dot{Q}_{amb} - \cancel{M_{z,s}\omega} = 0 \quad (1)$$

The design fan tip clearance is set to 50  $\mu\text{m}$ . However, for risk mitigation, the first tests use a 100  $\mu\text{m}$  shim (Figure 6) that increases the fan blade tip clearance to 150  $\mu\text{m}$ , yielding a relative running blade tip clearance of 0.071 ( $\frac{c_{4,n}}{b_{4,n}} = \frac{0.05+0.1-0.011}{1.82+0.05+0.1-0.011} = \frac{0.139}{1.959}$ ) at 168 krpm (nominal conditions) with the consideration of the thrust bearing clearance at hot conditions (11  $\mu\text{m}$ , green points in Figure 7). A high relative tip clearance decreases the fan efficiency due to increased tip leakage and reduces the fan pressure increase. An increased tip clearance also reduces the shroud torque ( $M_{z,s}$ ). The efficiency calculation assumes an adiabatic fan shroud, i.e., the viscous losses due to the shroud torque only increase the temperature of the fan fluid. Hence,  $M_{z,s}\omega$  in eq. (1) is approximately zero. The values obtained with numerical simulations suggest that the shroud torque power ( $M_{z,s}\omega$ ) may reach 5 % of the fan power for the non-throttled case (right black hexagram) of the 168 krpm speed line in Figure 13.

Both the leakage mass flow rate from the housing to the fan fluid domain and heat dissipation from the thrust bearing may affect the power and efficiency measurements significantly:

(1) The leakage mass flow rate from the pressurized housing (due to the turbine) towards the fan TE corresponds to the difference between the fan outlet and inlet mass flow rate ( $\dot{m}_l = \dot{m}_8 - \dot{m}_1$ ). The leakage flows from the housing through the in-ward pumping thrust bearing, and enters the fan impeller fluid domain at the TE (white arrows in Figure 6). Figure 13 shows the static housing pressure that is equal to to the total pressure (fluid velocity near zero), as well as the fan TE shroud pressure at 0°, 120°, and 240°. Since the fan power is deduced from the mass flow rate and temperature measurements, the leakage flow temperature has a direct impact on the measured fan power. If the leakage flow temperature is higher than the fan inlet temperature, the actual measurement overestimates the fan power, and thus underestimates the fan efficiency (and vice versa) for the case the fan inlet mass flow rate evaluates the fan power ( $P_{fan} = \dot{m}_1 (h_{t,8} - h_{t,1})$ ).

(2) The heat input to the fan impeller via conduction ( $\dot{Q}_{cond}$ ) has two main sources: (1) the heat conduction within the shaft because of a temperature gradient between the fan and the housing, as well as between the fan and the turbine. (2) The more dominant heat dissipation due to the losses of the journal bearings, the thrust bearings, and the shaft windage (Figures 6 and 9). This heat dissipation is directly linked to the viscous losses, and thus to losses that can be experimentally determined with a shaft run-out test. The heat conduction to the environment ( $\dot{Q}_{amb}$ ) in eq. (1) is approximately zero because of the glass fiber insulation.

As a consequence of this, this paper evaluates three different isentropic total-to-total fan efficiencies.

$$\eta_{is,1} = \frac{\dot{m}'_1 (h_{t,8,is} - h_{t,1})}{\dot{m}'_1 (h_{t,8} - h_{t,1})} = \frac{P_{is}}{P_1} \quad (2)$$

$$\eta_{is,2} = \frac{\dot{m}_1 (h_{t,8,is} - h_{t,1})}{\dot{m}_8 h_{t,8} - \dot{m}_1 h_{t,1} - \dot{m}_l h_{t,l}} = \frac{P_{is}}{P_2} \quad (3)$$

$$\eta_{is,3} = \frac{\dot{m}_1 (h_{t,8,is} - h_{t,1})}{\dot{m}_1 (h_{t,8} - h_{t,1}) - \dot{Q}_{cond}} = \frac{P_{is}}{P_3} \quad (4)$$

A fluid database evaluates the thermodynamic properties for dry air that is assumed as mixture of nitrogen, oxygen, and argon ( $\gamma_i = 0.78126, 0.2094, 0.00934$ ).

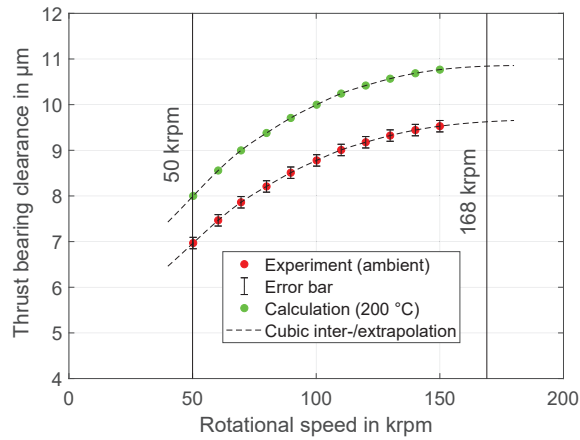
## EVALUATION OF THE LEAKAGE FROM THE TURBINE TO THE FAN

Figure 7 shows the shaft thrust bearing clearance ( $c_a$ ) as a function of the rotor rotational speed that is measured with a *LionPrecision* C3S capacitive probe at ambient conditions (red dots). The probe is mounted vertically above the fan spinner, which for these measurements is flat (black thick dotted line in Figure 6). At elevated temperatures, the viscosity of air increases; hence, the load capacity and stiffness of the bearing increase. Since no high-temperature-resistant, high-precision, and small-target-size-capable (target diameter is 4 mm) displacement sensor is available, the thrust bearing clearance can not be measured at the nominal conditions (200 °C). Figure 7 shows green dots that correspond to the calculated thrust bearing clearance at nominal conditions, assuming the same axial force for both the ambient and the nominal case (200 °C). The calculation utilizes the narrow-groove theory and the perturbation method [18]. The difference between the two cases is on the order of 1  $\mu\text{m}$ . Since space is limited, the thrust bearing clearance was only measured without the fan volute.

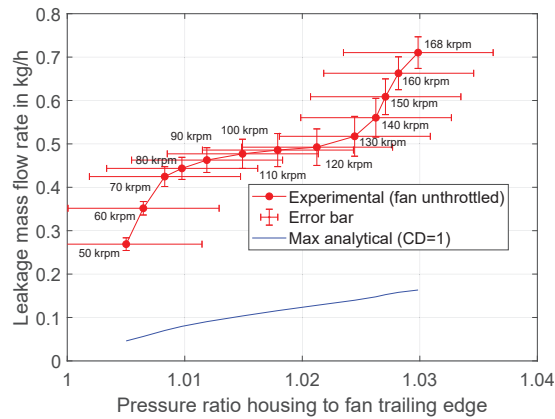
Figure 8 shows the measured leakage mass flow rate (red line) for the nominal conditions (air at 200 °C) and a non-throttled fan operation (right points of the speed lines in Figure 13). The measured leakage mass flow rate from the turbine to the fan is in the orders of several 0.1  $\text{kg h}^{-1}$ . The measurement is compared towards an analytical calculation based on a Laval nozzle that takes into account the thrust bearing clearance at nominal conditions (air at 200 °C, green dots in Figure 7), the total pressure and temperature in the housing ( $p_h$  and  $T_h$ ), and the average fan TE shroud pressure ( $p_{s,4}$ ). The blue line in Figure 8 shows this maximum possible leakage mass flow rate with a theoretical discharge coefficient of one ( $CD = 1$ ). This maximum leakage mass flow rate for the non-throttled fan is therefore below 0.2  $\text{kg h}^{-1}$ , and thus lower than 4 % of the fan inlet mass flow rate for all measured points between 50 krpm to 168 krpm. These results clearly suggest a significant discrepancy between the measurements and the theoretically maximum leakage flow rates. The authors hypothesize that this discrepancy is a consequence of residual swirl within the outlet side test section. As a consequence, the efficiency  $\eta_{is,2}$  from eq. (3) is evaluated using the calculated maximum possible leakage flow rate (blue line in Figure 8) instead of the measurements. The fan outlet mass flow rate is accordingly calculated with this maximum analytical value for the leakage mass flow rate and the fan inlet mass flow rate ( $\dot{m}_8 = \dot{m}_1 + \dot{m}_l$ ).

## EVALUATION OF THE HEAT DISSIPATION BY SHAFT LOSSES

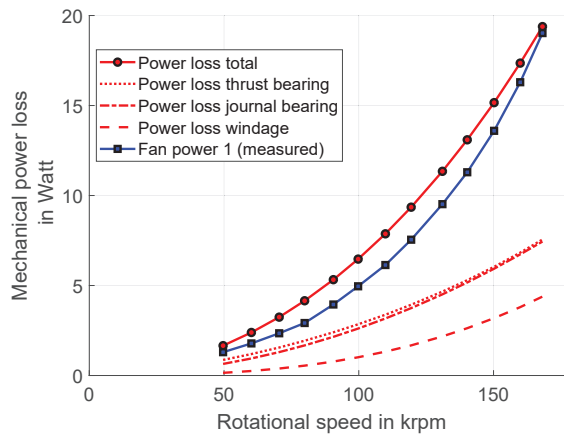
Above the lift-off speed, aerodynamic bearings operate without contact to the stator part. Nevertheless, the bearings yield losses due to the viscosity of the gas lubricant within the fluid film. Demierre et al. [19] compared an analytical windage loss model to rotor run-out measurements of a microrcompressor-turbine unit and it correlated within a  $\pm 10\%$  band. Figure 9 shows the analytical-calculated losses with respect to the rotational speed. The model suggests a total power loss of 19.4 W at a rotational speed of 168 krpm (red dots), consisting of the journal bearing losses of 7.4 W (dashed-dotted red line), the windage losses of 4.4 W (dashed red line), and the thrust bearing loss of 7.6 W (dotted red line). Figure 6 gives an overview of the losses close to the fan side: The thrust bearing consists of a plain part from a radius 5 mm to 8 mm and a grooved part from 8 mm to 9.4 mm (dotted line) and the journal bearing loss consists of both journal bearings (Figure 6 shows one journal bearing with a dashed-dotted line). The windage losses (dashed lines) consist of losses of the following components: (1) fan windage loss, (2) shaft windage loss (partially marked in Figure 6), and (3) windage losses at the turbine side (not shown in Figure 6).



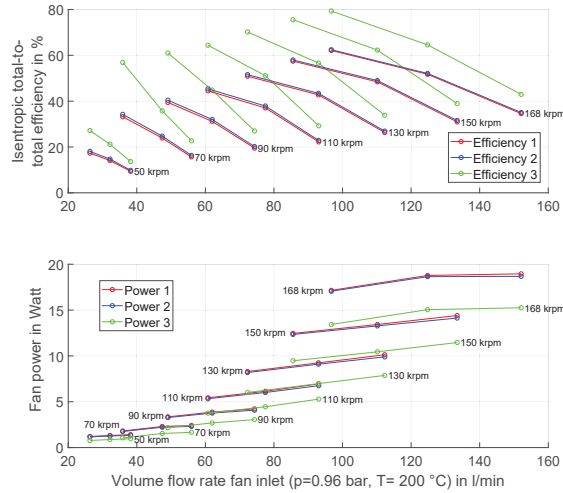
**GTP-19-1480-FIGURE 7.** MEASURED AND CALCULATED THRUST BEARING CLEARANCE ( $c_a$ ) WITHOUT MOUNTED FAN VOLUTE.



**GTP-19-1480-FIGURE 8.** COMPARISON OF EXPERIMENTAL AND ANALYTICAL ( $CD=1$ ) LEAKAGE MASS FLOW RATE FROM TURBINE TO FAN FOR THE NON-THROTTLED FAN OPERATION.



**GTP-19-1480-FIGURE 9.** CALCULATED LOSSES AND MEASURED FAN POWER AT 200 °C FOR THE MEDIUM THROTTLED CASE.



**GTP-19-1480-FIGURE 10.** COMPARISON OF DIFFERENT EFFICIENCY AND POWER DEFINITIONS.

### INFLUENCE OF LEAKAGE AND HEAT ON THE FAN POWER AND EFFICIENCY

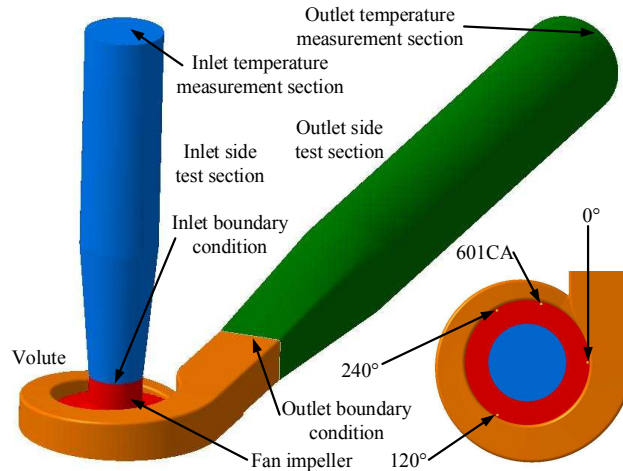
Figure 10 compares the measured isentropic total-to-total fan efficiencies and power as defined in eqs. (2) to (4). The experiments mean ambient pressure was  $0.965 \text{ bar} \pm 0.004 \text{ bar}$ , the total fan inlet temperature  $200 \text{ }^\circ\text{C} \pm 2 \text{ }^\circ\text{C}$ , and the rotational speed 50 krpm, 70 krpm, ..., 150 krpm, and 168 krpm  $\pm 1 \text{ krpm}$ . Correlations from ISO 5801 [15] adjust all experiments to a constant rotational speed, a constant ambient pressure (0.96 bar), and a constant fan inlet total temperature ( $200 \text{ }^\circ\text{C}$ ).

Isentropic efficiency 1 and power 1 according to eq. (2) are directly evaluated based on the measured data. The fan power is calculated with the measured fan inlet mass flow rate ( $\dot{m}_1$ ). Isentropic efficiency 2 and power 2 according to eq. (3) take the influence of the leakage mass flow rate into account. The leakage specific total enthalpy ( $h_{t,l}$ ) is determined using the housing temperature ( $T_h$ ) and the housing pressure ( $p_h$ ). It is assumed that this enthalpy is constant until the leakage flow enters the fan fluid domain at the fan TE. As pointed out in the previous section, the maximum theoretically possible leakage mass flow rate ( $\dot{m}_l$ ) with a discharge coefficient of 1 (blue line in Figure 8) is used. The fan outlet mass flow rate is calculated with this leakage mass flow rate ( $\dot{m}_8 = \dot{m}_1 + \dot{m}_l$ ). The influence of the leakage rate on the measured fan power and efficiency ranges between +1 % and +0.2 % and is thus very small. As a consequence, it is suggested that the effect of the leakage flow rate on the measurements can be neglected.

Isentropic efficiency 3 and power 3 according to eq. (4) account for the heat input from the thrust bearing losses. Here it is assumed that 50 % of the dissipated heat due to the axial bearing losses is conducted to the stator part, whereas the other 50 % of the heat is conducted to the fan impeller, and thus in the fan fluid domain. As shown in Figure 9 the heat dissipation ranges between  $0.9 \text{ W/2}$  at 50 krpm and  $7.6 \text{ W/2}$  at 168 krpm. With respect to the measured fan power (1.3 W at 50 krpm and 19.0 W at 168 krpm), the thrust bearing heat dissipation is suggested to have significant influence on power and efficiency measurements. Heat addition to the fan flow increases the measured fan power ( $P_1$ ), and thus decreases the measured isentropic fan efficiency ( $\eta_1$ ). While taking the heat addition effect into account, the net fan power is decreased ( $P_3$ ), and thus the isentropic fan efficiency with heat addition correction is increased ( $\eta_3$ ). The difference between  $\eta_1$  and  $\eta_3$  is 4.3 percentage points at 50 krpm and 23.7 percentage points at 70 krpm. Note that heat lost to the environment ( $\dot{Q}_{amb}$ ) that is neglected within this study would have the opposite effect. It would decrease the measured power ( $P_1$ ), and thus increase the measured efficiency ( $\eta_1$ ).

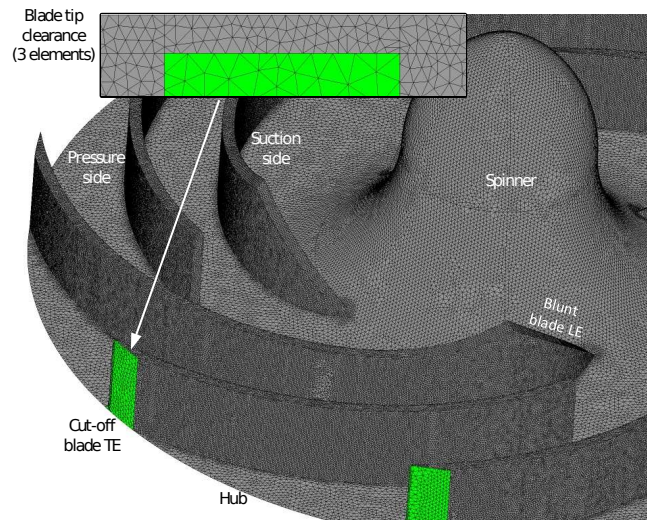
### NUMERICAL SIMULATION SETUP

A three-dimensional steady computational fluid dynamics (CFD) simulation with the commercial software *ANSYS CFX* simulates the fan performance that is compared to the experimental results. Figure 11 shows the entire fluid domain between the fan inlet and outlet temperature measurement locations: the inlet side test section (blue), the full fan impeller (red), the fan volute (orange), and the outlet side test section (green). The CFD simulation uses an unstructured mesh with 14.3 million tetrahedron elements for the fan (8 million) and volute domain (6.3 million). Figure 12 shows the mesh of the fan impeller domain (red domain in Figure 11). The geometry assumes the running clearance of  $140 \text{ } \mu\text{m}$  ( $150 \text{ } \mu\text{m} - 10 \text{ } \mu\text{m}$ ) at 168 krpm for all points. A fan impeller FEM simulation suggests that the



**GTP-19-1480-FIGURE 11.** FLUID DOMAIN OF THE MEASUREMENT (BLUE, RED, ORANGE, AND GREEN), FOR THE COMPUTATIONAL FLUID DYNAMIC SIMULATION (RED AND ORANGE), AND POSITION OF STATIC PRESSURE TAPS AT THE FAN TRAILING EDGE (0°, 120°, 240° AND THE BLADE PASSING FREQUENCY MEASUREMENT WITH A KISTLER 601CA).

axial blade elongation at the TE ranges between 3 μm to 10 μm, whereas it is nearly zero at the blade LE. As consequence, mechanical blade deformation is neglected. The 140 μm blade tip clearance is resolved with 3 elements within the gap. Figure 12 at the top left shows a detail of the tip clearance mesh at the fan blade cut-off TE. Correlations from ISO 5167 [16] evaluate the pressure loss at the bellmouth, and correlations from ISO 5801 [15] evaluate the pressure loss inside the fan inlet nozzle until the actual inlet of the CFD domain (red fan impeller domain). For example, this combined pressure losses is 0.36 mbar for the non-throttled case at 168 krpm, and thus very low. The fan impeller fluid domain is rotating with the corresponding rotational speed and features a frozen rotor fluid-to-fluid interface between the fan impeller outlet and the volute. The impeller shroud is a counter-rotating with respect to the rotating domain. At the inlet, a total temperature of 200 °C and a total pressure of 0.96 bar are specified corresponding to the experimental setup. At the outlet, the experimentally measured fan inlet mass flow rate is imposed (as stated before, the leakage effect is neglected). This measured fan inlet mass flow is adjusted to an inlet temperature of 200 °C, an inlet pressure of 0.96 bar, and the respective rotational



**GTP-19-1480-FIGURE 12.** MESH OF THE FAN IMPELLER WITH HUB, MAIN AND SPLITTER BLADES, AND A DETAIL OF THE BLADE TIP CLEARANCE AT THE BLADE CUT-OFF TRAILING EDGE.

speed (50 krpm, 70 krpm, ..., 150 krpm, and 168 krpm) as suggested in ISO 5801. All the wetted surfaces are considered as hydraulically smooth. Hence, surface roughness is not defined and skin friction loss is only caused by fluid viscosity. The area-averaged  $y$ -plus values inside the volute, impeller hub, impeller shroud, and impeller blades are maintained below nine, seven, 12, and five, respectively. All walls are modeled as adiabatic. The CFD uses a compressible and non-isothermal ideal gas (air). The advection scheme is set to high resolution. The SST turbulence model with a low turbulence intensity of 1 % at the inlet boundary is specified.

The total-to-total isentropic efficiency is evaluated between the inlet and outlet boundary as the mass-flow-averaged isentropic efficiency as defined in eq. (2) at the outlet boundary corresponding to the volute outlet. The total-to-total fan pressure rise is based on the mass-flow-averaged total pressure at the outlet boundary minus the ambient pressure of 0.96 bar and minus the calculated pressure loss of the inlet side test section. The pressure loss of the outlet side test section is therefore neglected. The fan TE shroud pressure corresponds to the area-averaged static pressure at the fan TE (diameter of 19.2 mm) minus the calculated pressure loss of the inlet side test section. The fan power is evaluated as the impeller torque (blades and hub) around the rotational axis multiplied with its angular velocity.

## COMPARISON OF THE EXPERIMENTAL RESULTS TOWARDS THE DESIGN POINT AND NUMERICAL RESULTS

Figure 13 shows the fan characteristic with the total-to-total isentropic efficiency ( $\eta_{is,1}$ ), the total-to-total fan pressure rise, the static gauge pressure at the fan impeller shroud at a diameter of 18.55 mm close to the fan TE for the  $0^\circ$ ,  $120^\circ$ , and  $240^\circ$  locations (Figure 11), the housing gauge pressure, as well as the fan power ( $P_1$ ). As stated before, correlations from ISO 5801 [15] adjust all experimental values to a constant rotational speed, a constant ambient pressure (0.96 bar), and a constant total fan inlet temperature ( $200^\circ\text{C}$ ).

The nominal speed line (168 krpm) has the same Mach number based on the total inlet conditions as the design case (SOFC anode off-gas consisting of water vapor, hydrogen, carbon monoxide, and carbon dioxide) and is therefore representative of the operation when coupled to the SOFC. A black dot marks the nominal design point. At nominal operation, the total-to-total pressure rise is 55 mbar and therefore 15 mbar lower than the specified fan total total pressure rise. This difference has three reasons: (1) Since the current test campaign features a  $100\mu\text{m}$  shim, the clearance is elevated; hence, the isentropic efficiency, and thus the fan pressure rise, is lower compared to the design clearance ( $50\mu\text{m}$ ). A numerical investigations with the design clearance of  $50\mu\text{m}$  suggests that the fan pressure rise increases by 25 mbar to 80 mbar. (2) For a fan inlet total pressure of 1.05 bar instead of 0.96 bar, the pressure rise is according to ISO 5801 [15] 87.5 mbar ( $\frac{1.05}{0.96}80\text{mbar}$ ). (3) The anode off-gas has a lower heat capacity ratio (1.3) than air (1.4); hence, the pressure rise is lower although the Mach number is constant. The pressure rise is therefore approximately equal to the initially specified 70 mbar with the design clearance ( $50\mu\text{m}$ ).

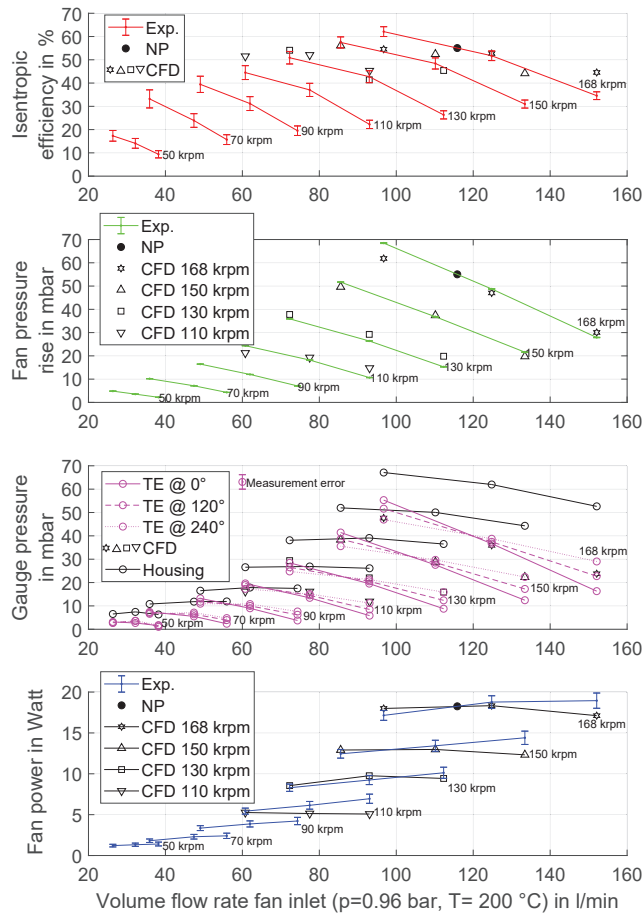
At the design point, the volute was designed with respects to conservation of the circumferential momentum ( $rc_u = \text{const}$ ) and constant volute pressure, which is in correlation with the experimental data, since the difference between the measured fan TE shroud pressure at  $0^\circ$ ,  $120^\circ$ , and  $240^\circ$  is nearly zero (magenta lines in Figure 13 at a constant speed line of 168 krpm). At higher mass flow rates, the fluid is accelerated within the volute, leading to a static pressure drop at  $0^\circ$  and a rise at  $240^\circ$  and vice versa for for lower mass flow rates.

With respects to the experiments and the CFD simulations, the fan TE shroud pressure, as well as the total-to-total fan pressure rise yield a good match for the nominal point (center point at 168 krpm), as well as for the non-throttled point (right point at 168 krpm). Near the nominal operation, the measured efficiency and power of the CFD simulation and the experiment correlate. The difference between the measured and simulated power is  $-0.3\text{ W}$  (1.6 %) and 0.9 percentage points for the isentropic efficiency. Both values are therefore within the measurement uncertainty.

For the non-throttled case, the difference in power is  $-1.8\text{ W}$  what is equal to  $-10\%$  with respect to the measured value. The measured efficiency 1 (34.6 %) is therefore 10 percentage points lower than the simulated value. The simulated value (44.6 %) is therefore near to isentropic efficiency 3 according to eq. (4) that is 43 %. Since the measured and simulated fan pressure rise and fan blade TE shroud pressure correlate, the authors assume the numerical simulation as valid at this non-throttled point. A heat input into the fan fluid control domain is thus not negligible. This heat input is favored due to high fan mass flow rates, which increase the heat transfer coefficient between the fan impeller and the fluid.

At the throttled point (left point on the nominal 168 krpm speed line) the steady CFD simulation does not fully capture the increasingly instationary fan flow. The difference of the total-to-total pressure rise is 5 mbar, whereas it is 4 mbar with respect to the simulated fan TE shroud pressure and the averaged measured value. The simulated fan power is within the measurement uncertainty. However, the simulated isentropic efficiency (54.4 %) is significantly lower than the measured one (62.1 %) due to the difference of the total-to-total pressure rise.

The turbine uses air at  $220^\circ\text{C}$  to drive the shaft, and thus the fan impeller. The higher the shaft power, the higher the turbine inlet pressure, the higher the expansion in the turbine, and the lower the turbine outlet temperature. Below rotational speeds of 120 krpm the turbine outlet temperature is higher than  $200^\circ\text{C}$ , and thus above the oven environment temperature and above the fan inlet temperature of  $200^\circ\text{C}$ . This involves mainly two effects: (1) The heat conduction from the turbine to the fan is increased, and (2) the dissipated heat due



**GTP-19-1480-FIGURE 13.** MEASURED FAN CHARACTERISTIC FROM EXPERIMENTS (EXP.) WITH THE RESPECTIVE MEASUREMENT UNCERTAINTIES, NOMINAL POINT (NP), AND COMPARISON TO CFD SIMULATION (CFD).

to bearing losses that is crossing the fan fluid domain is also increased, compared to an operation at rotational speeds above 120 krpm. The measured fan power and efficiency for rotational speeds at 50 krpm, 70 krpm, 90 krpm, and 110 krpm are therefore influenced by increased heat fluxes crossing the fan fluid domain. The difference in the isentropic efficiency is between seven percentage points for the throttled case up to 23.1 percentage points for the non-throttled case for the 110 krpm speed line. The center point and left point (throttled case) of the 130 krpm and 150 krpm speed line show better correlation. The simulated efficiency is within  $\pm$  four percentage points and the simulated power is within the measurement uncertainty, since the heat fluxes crossing the fan impeller domain are lower.

## CONCLUSION

A novel steam-driven anode off-gas recirculation (AOR) fan for a 10 kW<sub>e</sub> solid oxide fuel cell (SOFC) was designed, manufactured, coupled to a 6 kW<sub>e</sub> SOFC, experimentally characterized with air, and its performance compared to a computational fluid dynamics (CFD) simulation. This fan uses dynamic gas-lubricated bearings, more specifically herringbone-grooved journal and spiral-grooved thrust bearings that have proven to be reliable, even at elevated temperature of up to 220 °C. The design of the fan is based on a trade-off between efficiency and low manufacturing cost. Due to the high rotational speeds, the fan performance corresponds to the specified values, although the size is out of the common. The fan blade tip clearance is suggested to have a significant impact also for fans with relatively low pressure rises.

At the nominal point at 168 krpm, the measured inlet mass flow rate is 4.9 kg h<sup>-1</sup>, the total-to-total pressure rise reaches 55 mbar, yielding an isentropic total-to-total efficiency 55 %, and a power of 18.3 W.

The influence of leakage mass flow rate from the housing to the fan trailing edge causes a theoretical maximum deviation in the measured isentropic total-to-total efficiency between 0.2 and 1 percentage points and can therefore be neglected within the experiments and simulations. A possible heat input to the fan fluid domain due to the thrust bearing losses has the potential of influencing the total-to-total isentropic efficiency measurement by up to 24 percentage points and is therefore not negligible. An adiabatic CFD simulation is compared to the measurements.

At the nominal point, the difference between the experimentally measured and simulated values for the isentropic total-to-total efficiency is +0.9 percentage points, for the fan power -0.3 W, for the fan total-to-total pressure difference -0.7 mbar, and for the averaged static pressure at the fan trailing edge -1.7 mbar. It is thus concluded that the proposed experimental set up is suitable for characterizing the fan at the nominal operational point, although its power is in the same order as the shaft losses. At this point, the majority of the dissipated heat cross a heat sink that is the cold turbine fluid domain in this case. An insulation with glass fiber tapes and a PTFE tube reduce the heat conduction to the (oven) environment. However, at off-design conditions, the dissipated heat has significant impact. The precise determination of the entire fan characteristic remains therefore challenging.

## ACKNOWLEDGMENT

The authors acknowledge the research grant from the Canton de Vaud under the “100 million de francs pour les energies renouvelables et l’efficacite energetique”.

## REFERENCES

- [1] SOLIDpower, 2016. BlueGen datasheet. [http://www.solidpower.com/fileadmin/user\\_upload/pages/Logos\\_materialien/SOLIDpower.BlueGEN.Brochure.UK.web.pdf](http://www.solidpower.com/fileadmin/user_upload/pages/Logos_materialien/SOLIDpower.BlueGEN.Brochure.UK.web.pdf). Accessed: 2018-06-16.
- [2] Jülich Forschungszentrum, 2017. Anniversary for Jülich’s Slow Burner: Fuel Cell Running for 10 Years. <https://www.fz-juelich.de/SharedDocs/Pressemitteilungen/UK/EN/2017/2017-08-07-jubilaem-sofc.html>. Accessed: 2018-06-22.
- [3] Wagner, P. H., Wuillemin, Z., Diethelm, S., Van herle, J., and Schiffmann, J., 2017. “Modeling and Designing of a Radial Anode Off-Gas Recirculation Fan for Solid Oxide Fuel Cell Systems”. *Journal of Electrochemical Energy Conversion and Storage*, **14**(1), May, pp. 011005–011005–12.
- [4] Peters, R., Engelbracht, M., Tiedemann, W., Hoven, I., Deja, R., Nguyen, V. N., Blum, L., and Stolten, D., 2017. “Development and Test of a Solid Oxide Fuel Cell Subsystem with a Low Temperature Anode Off-Gas Recirculation”. *ECS Transactions*, **78**(1), May, pp. 2489–2495.
- [5] GE Power, 2018. Breaking the Power Plant Efficiency Record...Again! <https://www.ge.com/power/about/insights/articles/2018/03/nishi-nagoya-efficiency-record>, Mar. Accessed: 2019-02-25.
- [6] Powell, M., Meinhardt, K., Sprenkle, V., Chick, L., and McVay, G., 2012. “Demonstration of a highly efficient solid oxide fuel cell power system using adiabatic steam reforming and anode gas recirculation”. *Journal of Power Sources*, **205**, May, pp. 377–384.
- [7] Tanaka, Y., Sato, K., Yamamoto, A., and Kato, T., 2013. “Development of Anode Off-Gas Recycle Blowers for High Efficiency SOFC Systems”. *ECS Transactions*, **57**(1), Oct., pp. 443–450.
- [8] Balje, O. E., 1981. *Turbomachines : a guide to design, selection and theory*. Wiley, New York etc.
- [9] Rechberger, J., Reissig, M., and Hauth, M., 2013. “AVL SOFC Systems on the Way of Industrialization”. *ECS Transactions*, **57**(1), Oct., pp. 141–148.
- [10] Agrawal, G., 2010. Advances in fuel cell blowers. [www.netl.doe.gov/file%20library/events/2009/seca/presentations/Agrawal\\_Presentation.pdf](http://www.netl.doe.gov/file%20library/events/2009/seca/presentations/Agrawal_Presentation.pdf). Accessed: 2015-04-14.
- [11] Heshmat, H., 2016. High Temperature Anode Recycle Blower for Solid Oxide Fuel Cell. Tech. rep., Mohawk Innovative Technology, <https://www.netl.doe.gov/research/coal/project-information/proj?k=FE0027895>. Accessed: 2018-08-16.
- [12] Wagner, P. H., 2019. “Integrated Design, Optimization, and Experimental Realization of a Steam-Driven Micro Recirculation Fan for Solid Oxide Fuel Cell Systems”. PhD thesis, EPFL, Lausanne. Thesis number 9337.
- [13] Bruno Eck, 2003. *Ventilatoren : Entwurf und Betrieb der Radial-, Axial- und Querstromventilatoren*, 6. aufl. ed. Springer, Berlin etc.
- [14] Leidel, W., 1967. “Einfluß von Zungenradius und Zungenabstand auf Kennlinie und Geräusch eines Radialventilators”. PhD thesis, TU Berlin.
- [15] ISO, 2007. ISO 5801: Industrial fans - Performance testing using standardized airways.
- [16] ISO, 2003. ISO 5167: Measurement of fluid flow by means of pressure differential devices inserted in circular cross-section conduits running full.

- [17] VDI, 1991. VDI/VDE 2041: Measurement of Fluid Flow with Primary Devices - Orifice Plates and Nozzles for Special Applications.
- [18] Schiffmann, J., 2008. "Integrated design, optimization and experimental investigation of a direct driven turbocompressor for domestic heat pumps". PhD thesis, EPFL, Lausanne. Thesis number 4126.
- [19] Demierre, J., Rubino, A., and Schiffmann, J., 2014. "Modeling and Experimental Investigation of an Oil-Free Microcompressor-Turbine Unit for an Organic Rankine Cycle Driven Heat Pump". *Journal of Engineering for Gas Turbines and Power*, **137**(3), Oct., pp. 032602-1-032602-10.